NANO LETTERS

Letter

pubs.acs.org/NanoLett

Nanomechanical Torsional Resonators for Frequency-Shift Infrared Thermal Sensing

X. C. Zhang,[†] E. B. Myers,[†] J. E. Sader,[†,‡] and M. L. Roukes*[,†]

[†]Kavli Nanoscience Institute and Condensed Matter Physics, California Institute of Technology, MC149-33, Pasadena, California 91125, United States

[‡]Department of Mathematics and Statistics, The University of Melbourne, Victoria 3010, Australia

Supporting Information

ABSTRACT: We investigate use of nanomechanical torsional resonators for frequency-shift-based infrared (IR) thermal sensing. Nanoscale torsion rods, ~1 μm long and 50−100 nm in diameter, provide both extraordinary thermal isolation and excellent angular displacement and torque sensitivities, of order $\sim 10^{-7}$ rad·Hz$^{-1/2}$ and $\sim 10^{-22}$ (N·m) Hz$^{-1/2}$, respectively. Furthermore, these nanorods act as linear torsional springs, yielding a maximum angular displacement of 3.6° and a dynamic range of over 100 dB; this exceeds the performance of flexural modes by as much as 5 orders of magnitude. These attributes lead to superior noise performance for torsional-mode sensing. We demonstrate the operational principles of torsional-mode IR detection, attaining an uncooled noise equivalent temperature difference (NETD) of 390 mK. By modeling the fundamental noise processes, we project that further reduction of device size can significantly improve thermal responsivity; a room-temperature NETD below 10 mK appears feasible.

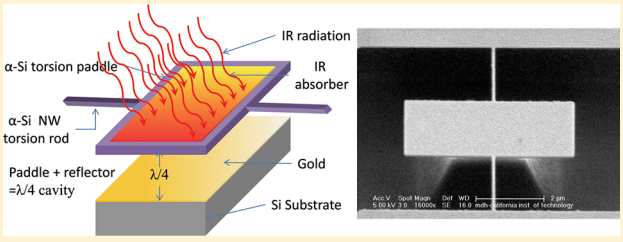

KEYWORDS: *Nanoelectromechanical systems, torsional resonator, infrared sensor, thermal imaging*

Nanoelectromechanical systems (NEMS) show promise for state-of-the-art applications in mass sensing (single-molecule mass spectroscopy),[1] force transduction (magnetic-force single spin detection),[2] and explorations of the quantum regime of mechanical modes.[3] In many of these applications, the minute signal under study is transduced within the NEMS device through the resulting resonance frequency shift it induces. This transformation takes advantage of the unprecedented sensitivities that NEMS provide, which arise from their extremely high resonance frequencies, minuscule active masses, very small force constants, and high quality factors (Qs).

There exist several studies employing microelectromechanical systems (MEMS) for temperature sensing applications,[4,5] including IR detection based on either the deformation of a bimorph[6,7] or the frequency-shift effect[8] upon temperature rise. Nevertheless, using the frequency shift for thermal sensing has not yet been investigated in the realm of NEMS.[9] The miniaturized scale of NEMS enables great thermal isolation, minute heat capacity and hence unprecedented thermal sensitivity, and eventually a reduced size IR focal plane array that substantially reduces the cost of the germanium IR imaging optics.

In this Letter, we propose and experimentally implement a frequency-shift IR bolometer based on a micrometer size torsional resonator with nanoscale supporting rods. Our study reveals a superior dynamic range (DR) and frequency stability for operation based on the torsional mode as compared with flexural modes. Our detailed modeling shows that the thermal responsivity increases with downscaling device dimensions with a NETD below 10 mK ultimately feasible for room-temperature operation. For our first experimental realization of this design reported here, we demonstrate a NETD of 390 mK for the torsional mode; this is comparable with state-of-the-art MEMS based IR detectors based on other transduction mechanisms.[6,10,11]

A schematic of our torsional frequency shift IR bolometer is illustrated in Figure 1a. A torsional paddle, coated with a thin layer of IR absorbing material, acts as the top of a quarter-wavelength ($\lambda/4$) cavity formed with a metallic ground plane underneath. It is constructed using a material with a low thermal conductivity κ, such as amorphous silicon (α-Si) for which a κ = 0.1 W/(m·K) has been reported.[12] Together with the nanoscale supporting rods, very significant thermal isolation of the paddle is attained. The absorber can be formed using, for example, a nanometer-scale thickness TiN film, which is known to have good IR absorption,[13] while not overloading the heat capacity of the system. The $\lambda/4$ cavity positions the antinode of the IR standing wave at the location of the paddle and can yield IR absorption close to 100%. Efficient IR absorption acts to heat the paddle to a temperature above ambient, thereby causing a measurable resonance frequency shift of the device.

The thermal responsivity of our frequency shift IR bolometer can be analyzed as follows. If G denotes the thermal conductance through the supporting rods, C is the heat

Received: December 19, 2012
Revised: February 14, 2013

   dx.doi.org/10.1021/nl304687p | *Nano Lett.* XXXX, XXX, XXX−XXX

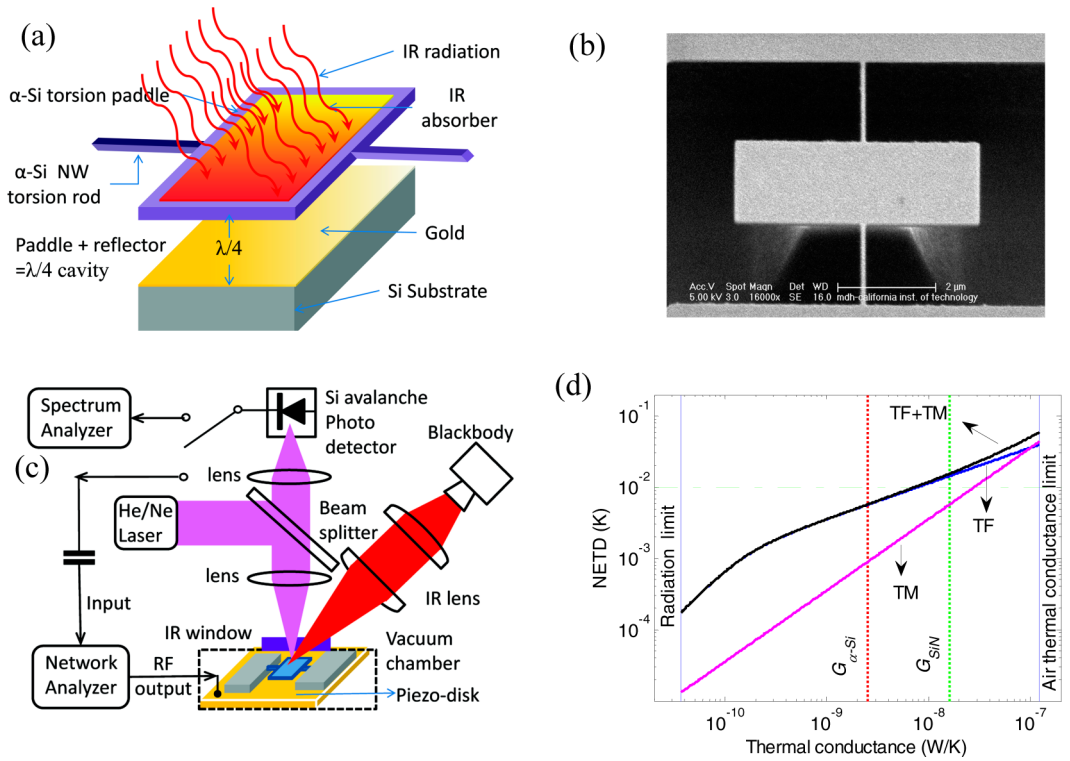

Figure 1. (a) Schematic layout of a torsional-frequency-shift-based IR detector. (b) A scanning electron microscope image of a torsional device. (c) Schematic optical interference setup used to detect the resonant frequency shift of the device upon IR radiation. (d) Calculated NETD versus the thermal conductance. The "TM", "TF", and "TM + TF" labeled curve represents the thermomechanical noise, the temperature fluctuation noise limited, and total NETD. The left vertical line is the lowest thermal conductance set by the thermal radiation limit. The right vertical line is the upper limit of the thermal conductance set by the air gap underneath the device paddle. The vertical dashed line denotes the thermal conductance if the rod material is α-Si and SiN with a thermal conductivity of 0.5 and 3.2 W/(m·K), respectively.

capacity of the sensitive volume, and P_0 is the IR radiation power impinging on the paddle that is modulated with frequency ω_m, then the temperature rise of the sensitive area will be $\Delta T = (\eta P_0)/[G((1+\omega_m^2\tau^2)]^{1/2}$,[14] where η is the fraction of the incident IR power absorbed, and $\tau = C/G$ is the time constant characterizing the thermal response. From the definition of the temperature coefficient of frequency shift TCF $= (1/f)[(df)/(dT)]$, where f is the device resonant frequency. The responsivity R, which represents the frequency shift induced by power absorption, can be expressed as

$$R = \frac{\Delta f}{P_0} = \frac{\eta(\mathrm{TCF} f_0)}{G\sqrt{(1+\omega_m^2\tau^2)}} \quad (1)$$

The mode-dependent TCF formulas for a stressed torsional resonator, derived in the Supporting Information, can be expressed as follows

$$\text{Flexural mode TCF} = \frac{\alpha+\beta}{2} - \frac{3}{5}\left(\frac{l}{h}\right)^2\alpha \quad (2a)$$

$$\text{Torsional mode TCF} = \frac{\alpha+\beta}{2} \quad (2b)$$

Here $\alpha = (1/l)[(dl/dT)]$ is the linear thermal expansion coefficient, $\beta = (1/E)[(dE/dT)]$ is the temperature coefficient of Young's modulus E, and l and h are the length and thickness of the torsion rods, respectively. For a silicon nitride (SiN) film, $\alpha = 3 \times 10^{-6}$ K^{-1} and $\beta = -4.8 \times 10^{-5}$ K^{-1}.[4] Note that the TCF of the flexural mode possesses an additional term $-(l/t)^2\alpha$. This geometric factor, which is enhanced for structures with a large aspect ratio, originates from the thermally induced stress, denoted as $\sigma_{th} = -\alpha E \Delta T$. This thermal stress has a component along the direction of motion of the flexural mode and thus acts to soften its spring constant (see Figure S1 of Supporting Information) and change its resonant frequency (see Supporting Information eq S14). By contrast, the thermal stress is parallel to the torsional axis and hence generates zero torque. Accordingly, thermal stress has negligible influence on the resonant frequency of the torsional mode. Equations 2a and 2b qualitatively agree with the experimentally measured TCF values displayed in Figure 5a.

Upon a uniform downscaling of all dimensions by a common factor, the resonant frequency f_0 will be increased by the same factor, as will the thermal resistance $1/G = l/\kappa A$; A is the cross sectional area of the supporting rod. Hence, according to eq 1, the frequency-shift-based thermal responsivity, R, will scale inversely with linear dimension squared. This favorable scaling gives NEMS devices their advantageous thermal responsivity compared to MEMS. The scaling law should also apply for a structures patterned from composite materials where the parameters, E, density ρ, stress σ, and α, can be replaced with effective values that represent weighted averages of the two materials.[9]

The ultimate sensitivity of our frequency-shift-based detector is limited by various frequency noise processes, of either intrinsic or extrinsic origin.[15] We concentrate on three fundamental limits: the radiation background fluctuations, temperature fluctuations, and thermomechanical noise.

All thermodynamic systems are subject to energy fluctuations with the environment, given their finite thermal conductance

dx.doi.org/10.1021/nl304687p | Nano Lett. XXXX, XXX, XXX−XXX

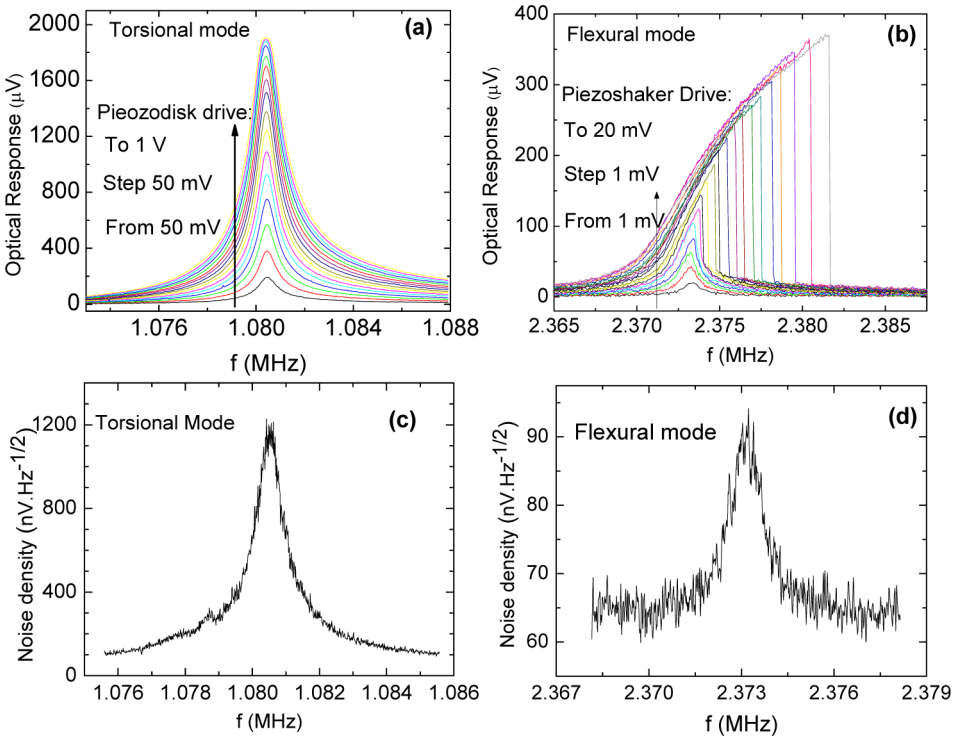

Figure 2. Optically detected resonances at various actuation levels for the torsional (a) and flexural (b) mode, and the associated thermomechanical noise spectrum measured for the torsional (c) and flexural mode (d).

and heat capacity. These energy fluctuations are manifested as temperature fluctuations, their mean square value, integrated over all frequencies, is $\overline{\Delta T^2} = (4k_B T^2/C)$,[15] where k_B is the Boltzmann constant. The smaller the device (hence smaller C), the more severely will frequency stability be compromised by this temperature noise.

NETD is defined as the minimum resolvable temperature difference within an imaged scene. It depends on the intrinsic properties of the detector, but also on the detector assembly's efficiency to capture the IR radiation emanating from the scene (see eq S26 in Supporting Information.) The limitation to NETD imposed by temperature fluctuations is depicted by the "TF" labeled curve in Figure 1d (see details in Supporting Information). As expected, a lower G or better thermal isolation yields a lower NETD. In ambient conditions, the maximum achievable thermal isolation is limited by the air beneath the paddle. In vacuum, the ultimate lowest thermal conductance is set by the radiation law $G_{rad} = 4\varepsilon_{SiN}A_d\sigma_T T^3$, where $\varepsilon_{SiN} = 0.6$ is the emissivity of SiN, A_d is the detector sensitive area, and σ_T is the Stephan–Boltzmann constant.

Thermomechanical noise also imposes a fundamental limit to the device's frequency stability. It induces fluctuations in the resonator's position at finite temperatures, thus imposing a fundamental limit on the displacement sensitivity of the device. Thermal displacement fluctuations with a spectral density $S_x(\omega)$ generate phase fluctuations $S_\phi(\omega) = S_x^2(\omega)\langle x\rangle^2$, and in turn frequency fluctuations $S_\omega(\omega) = [\omega_0/(2Q)]^2 S_\phi(\omega)$ with a spectral density of $S_\phi(\omega)$ and $S_\omega(\omega)$, respectively. Here $\langle x\rangle$ is the rms of the resonator amplitude and ω_0 is the resonant angular frequency. The frequency fluctuations caused by thermomechanical noise are represented as $\delta\omega_0 = \{[(k_B T)/(E_c)](\omega_0 BW)/Q\}^{1/2}$,[16] where E_c is the carrier energy and BW is the measurement bandwidth. For the torsional mode, we have $E_c = I\omega_0^2\langle\theta_c^2\rangle$, where I is the moment of inertia, and θ_c is the displacement angle of 3.6° (the maximum value observed with our device, see below). These frequency fluctuations $\delta\omega_0$ can be referred back to the input domain and represented as equivalent power fluctuations, $\delta P_{TM} = G\delta\omega_0/(\omega_0 TCF)$. The NETD limited by such thermomechanical noise processes is labeled by "TM" in Figure 1d. We assume values of TCF = 0.01% and f_0 = 10 MHz in our calculations.

The total NETD = $[(NETD_{TF})^2 + (NETD_{TM})^2]^{1/2}$ is shown by the black curve in Figure 1d. The actual thermal conductance of the device is shown by the two vertical dashed lines, where we assume a thermal conductivity of 0.5 and 3.2 W/(m·K) for α-Si and SiN, respectively.[17,18] It is apparent that attaining a NETD below 10 mK is feasible.

Microscale torsional resonators have been employed in applications such as optical mirrors in digital light processing (DLP) technology,[19] switches, intensity, and/or phase modulators.[20] Compared with their microscale counterparts, there have been relatively few studies of nanoscale torsional resonators. Evoy et al. report micrometer-scale silicon torsional devices.[21] The smallest torsional devices reported are those that incorporate a carbon nanotube tube (CNT) as the torsional spring for a submicrometer size metal paddle.[22] These devices exhibit appealing properties including an unusually large deflection angle of 180°[23] due to the extremely soft spring constant (κ) ~3 × 10^{-18} N·m,[23,24] a torsional piezoresistive effect,[25,26] and electrically detected torsional resonances.[27,28] Nevertheless, their Qs are low, only in the range of 78–250[27,28] and they suffer from the fact that it is very problematic to implement large-scale integration of these devices to make pixel arrays. Their soft torsion spring also results in a high angular displacement noise floor of 3°,[23] consequently yielding a rather limited dynamic range of only ~35 dB. In this work, we report dynamic properties of SiN-based torsional resonators with nanoscale supporting rods, with particular focus on their

dx.doi.org/10.1021/nl304687p | Nano Lett. XXXX, XXX, XXX–XXX

superior torque and angular displacement sensitivities, dynamic range, frequency stability, and thermal sensitivities for IR detection.

Our torsional resonators are made from 100 nm thick low stress SiN grown by low pressure chemical vapor deposition (LPCVD) onto a Si substrate (fabrication details are presented in Supporting Information). Each of the supporting rods is 50−100 nm wide, 2 μm long, and its paddle is 2 μm wide and 5 μm long. The devices are mounted on piezoceramic disks for actuation and are characterized by laser interferometric displacement detection that is schematically shown in Figure 1c. The IR radiation from the blackbody is focused by an IR lens through a ZnSe window onto the sample that is housed within a vacuum chamber. The chamber is evacuated below a 10^{-5} Torr pressure to exclude damping and heat conduction effects through the air.

The driven torsional and flexural resonances are depicted in Figure 2 panels a and b, respectively. What is most immediately evident from the flexural mode is its mechanical nonlinearity onset occurring at a several millivolt actuation. We are able to record the thermomechanical noise spectra of both modes. The torsional mode (Figure 2c) exhibits 1 order of magnitude higher noise spectral density than the flexural mode (Figure 2d); this is a combined result of the soft torsional spring constant, the paddle length, and the location of the laser spot on the paddle.

The torsional angular displacement noise spectral density can be expressed as $S_\theta^{1/2} = [(4k_BTQ)/(\omega_0\kappa)]^{1/2}$, where $\kappa = 2KG_s/L$ is the torsional spring constant, G_s is the shear modulus, and K is the torsional moment of inertia expressed in Supporting Information eq S21. It can be experimentally determined by $\kappa = \omega_\theta^2 I$. Using the expression of $S_\theta^{1/2}$, an angular displacement resolution of 1.18×10^{-7} rad.Hz$^{-1/2}$ is obtained. Details of our calculation can be found elsewhere.[29] The torque thermomechanical noise spectral density is $S_T^{1/2} = S_\theta^{1/2}(\kappa/Q) = [(4k_BT\kappa)/(\omega_0 Q)]^{1/2}$. Following similar procedures, a torque resolution on the order of 10^{-22} (N·m) Hz$^{-1/2}$ is obtained. Table 1 summarizes the analyzed results for both modes.

Table 1. Parameters of the Torsional and Flexural Modes of a Torsional Resonator

quantity\mode	torsional	flexural
Q	1555 (92)[a]	2466 (92.2)[a]
(angular) displacement resolution	1.18×10^{-7} rad Hz$^{-1/2}$	2.33×10^{-12} m Hz$^{-1/2}$
torque (force) resolution	1.72×10^{-22} (N.m) Hz$^{-1/2}$	5.19×10^{-16} N Hz$^{-1/2}$
max. (angular) displacement achieved	>3.6°	X
dynamic range (db)	≥100	58

[a]The value in the bracket indicates Q in air.

The dynamic range (DR) of NEMS is the ratio of its largest linear amplitude and the rms of the amplitude noise floor S_x. Typically expressed in in decibels, it specifies the linear operating range of the device. For a flexural mechanical resonator, it is formulated as DR(dB) = 20 log$[0.745x_{nc}/(2S_xBW)^{1/2}]$,[30] where $0.745x_{nc}$ is the 1 dB compression point of the onset of the nonlinear resonance. On the basis of the data in Figure 2, the flexural dynamic range is determined to be 58 dB.

For torsional vibrations studies of dynamic range are hampered by the inherent nonlinearity of the optical transduction technique, which has many experimental manifestations. Figure 3b shows the torsional amplitude initially linearly increasing with the actuation. At a critical drive, the resonance amplitude saturates and starts to split into doublet peaks. The splitting gradually grows with the actuation but with the peak height staying constant. This is more evident in the color-scale plot in the inset of Figure 3c. Figure 3a shows the center resonance amplitude versus the actuation power in the logarithmic scale for another device. A linear response below 20 dBm actuation evolves into a down turning behavior at higher powers. The same data linearly plotted in the top left inset can be precisely fitted by a sinusoidal function. All these findings are indications of the linearity of the torsional motion, elaborated by the simple model presented below. The conclusion of this analysis is that the devices in Figure 3 are actually in their linear operation region over the whole power range explored. The dynamic range of the device in Figure 3a can thus be estimated to be 100 dB, based on the thermomechanical noise spectrum in the lower right inset.

We find that the optical nonlinear effect in our experiment can be accounted for by a simple interference model (see Supporting Information). When the device vibrates at an amplitude x, the laser interference intensity, $I(r)$, becomes modulated. The modulation depth in $I(r)$, ΔI recorded by the photodetector provides measure of the device resonant amplitude, that is, the optical displacement signal

$$\Delta I = 4A_0 \sin(2kd)\sin(2kx) = A_1 \sin(2kx) \tag{3}$$

Here d is the interference cavity separation, k is the wave vector of the laser light, and A_0 and A_1 are constants. Equation 3 justifies the sinusoidal dependence in the top inset of Figure 3a. It also suggests that the displacement signal will reach a maximum when $2kx = \pi/2$, that is, $x = \lambda/8$. Thus, the split, constant-height peaks in Figure 3b are positions where the resonator's amplitude reaches $\lambda/8$ on both sides of its center resonance.[31] We further quantify the splitting versus the actuation level based on a driven damped harmonic resonator model (see Supporting Information)

$$\Delta\omega = \frac{\omega_0}{Q}\sqrt{\left(\frac{x}{x_c}\right)^2 - 1} = \frac{\omega_0}{Q}\sqrt{\left(\frac{V}{V_c}\right)^2 - 1} \tag{4}$$

V is the RF voltage applied on the piezodisk, which acts as a linear actuator in the power range of this work. V_c is the RF voltage when $x_c = \lambda/8$. Plotted in Figure 3c, the splittings versus actuation voltages show an almost perfect square-root law, as described by eq 4. The maximum attained amplitude is approximately $a_{max} = 2x_c = \lambda/4$. Assuming the laser spot shines in the proximity of the paddle edge, which is 2.5 μm away from the torsional axis, the maximum torsional angle is 3.62°. The thermomechanical noise spectrum yields an angular noise floor about 1.55×10^{-5} degree. Thus, the dynamic range of this second device is 107.4 dB, which is comparable with the device in Figure 3a.

The above experiments unambiguously demonstrate the linear nature of the torsional mode despite the artifacts caused by the optical nonlinearity. While nonlinear Duffing behavior of the torsional mode has been reported in previous studies, these nonlinearities appear to originate either from the electrostatic driving and detection method,[32] or by the increase of the

dx.doi.org/10.1021/nl304687p | Nano Lett. XXXX, XXX, XXX−XXX

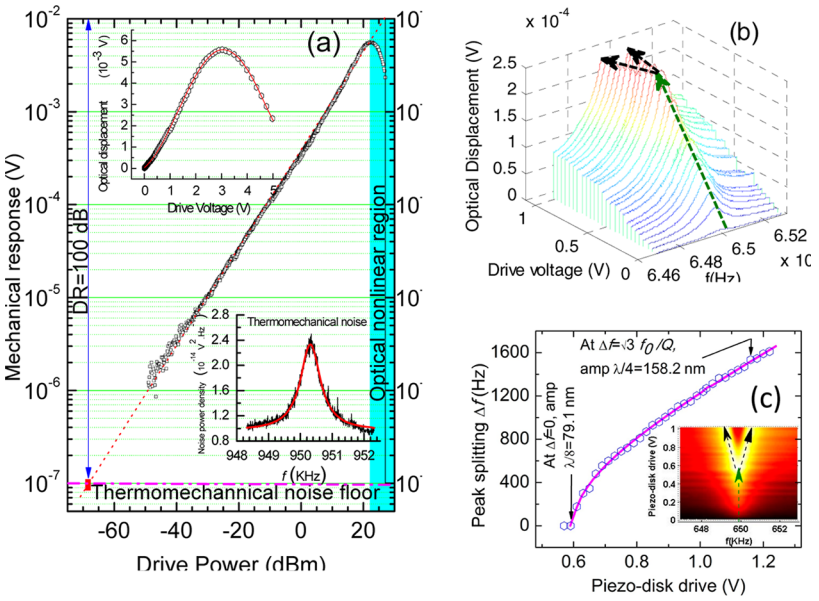

Figure 3. Investigation of the dynamic range of the torsional mode. (a) The center resonance amplitude versus the piezodisk drive power. The initial linear response is followed by a downturning behavior at higher drive levels, as shown inside the shaded (cyan) box. The top left inset shows the same data but in the linear scale with a sinusoidal fit denoted by the red curve. The thermomechanical noise spectrum is shown in the bottom right inset with the Lorentzian fit in red. (b) Waterfall plot of resonances at different drives for another device. Initially the resonance amplitude linearly grows with the drive, indicated by the olive arrowed line. Afterward it splits into two peaks with constant peak heights, shown by the two black arrowed lines. This process is more obvious in the color-scale plot in the inset of (c). The frequency splitting versus the drive voltage can be modeled by a square root law as shown in (c).

intershell coupling in the multiwalled CNT torsional rod.[27] As such, they are not applicable to our devices.

In our torsional devices with ~100 × 100 nm^2 cross sectional supporting rods, the torsional dynamic range is 40−50 dB higher than that of the flexural mode. Theory predicts a dependence of the dynamic range on $D[(D/L)^5]^{1/2}$ [30] and $(D^7L)^{1/4}$ for the flexural and torsional mode (see Supporting Information), respectively, where D is the diameter and L is the length of the supporting rods. The torsional dynamic range degrades much more slowly as the rod diameter is reduced. Increasing the rod length L, which is favorable for enhancing thermal isolation, will give an advantageous torsional dynamic range but will adversely affect the flexural DR.

We compare the frequency stability of both modes in the time domain, as characterized by their Allan deviation (AD).[33] The device in Figure 4a has 100 nm thick and 80 nm wide supporting rods, while a more "bulky" device with 500 nm thick and 200 nm wide rods is shown in Figure 4b. Their paddles are the same area (2 × 5 μm^2) except they have different thicknesses. The AD is the root of the time variance of the measured frequency of a source, each measurement averaged over a time interval τ_A. Its definition and the measurement method are described in Supporting Information.

The measured ADs at τ_A = 1 s are plotted in Figure 4 as a function of device amplitude (characterized by the optical displacement signal in volts). The thicker device possesses an Allan deviation that is over 1 order of magnitude better. At τ_A = 1 s, the frequency fluctuations are dominated by white noise processes originating from either thermomechanical or photodetector shot noise, as the inset of Figure 4b indicates. By shrinking the device size from Figure 4 panel b to panel a, the torsional and flexural AD suffers from 1 and 2 orders of magnitude degradation, respectively. The less severe reduction of the torsional AD is correlated with its wider DR, evidenced

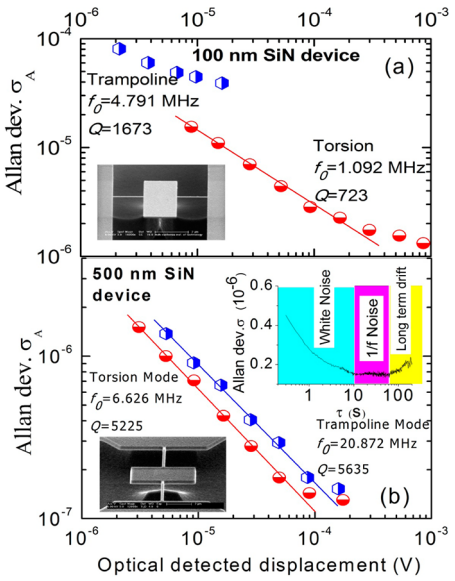

Figure 4. Allan deviations (at an interval time τ_s = 1 s) versus the optically detected resonance amplitude (in volts) for the torsional and flexural mode for a 100 nm thick, 80 nm wide rods (a), and 500 nm thick, 200 nm wide rods SiN device (b). Their paddles are the same area of 2 × 5 μm. The inset of (b) shows an exemplary curve of Allan deviation as a function of interval time.

by a wider data range on the x-axis of Figure 4a. The x-data range represents the device's practical working zone. Further actuating the device above this range is hampered by the mechanical or the optical transduction nonlinearity for the flexural and torsional mode, respectively.

We have also studied the TCFs of both modes. There are two types of devices investigated in this study: one has 10 nm thick gold film only on the paddle while the rod is pristine SiN;

dx.doi.org/10.1021/nl304687p | Nano Lett. XXXX, XXX, XXX−XXX

and the other has 12 nm thick gold film covering the whole surface. The focused laser can generate local heating to induce a frequency shift of the device. The laser power is varied between 0.125 and 1.25 mW with the resulting mode-dependent relative frequency shifts listed in Table 2. Since the temperature distribution profile remains identical during the measurement, we can infer that the flexural mode possesses a 6−8 fold larger TCF than the torsional mode.

Table 2. Relative Frequency Shift $(\Delta f)/f$ When Incident Laser Power Increases from 0.125 to 1.25 mW

sample	torsional (%)	flexural (%)	$TCF_{flex}/TCF_{Torsion}$
gold only on paddle	−0.38	−3.1	8.16
gold all over	−0.039	−0.26	6.67

We have also quantitatively measured the TCF by applying Joule heating to the device through the thin gold film overlayer. The applied voltages are converted into temperatures by finite element method (FEM) simulations. The obtained TCFs in Figure 5a are 92 and 548 ppm·K^{-1} for the torsional and flexural mode, respectively. Figure 5b is the color-scale plot of the temperature profile at a bias of 0.056 V. As expected, the paddle is at a uniform temperature of 329.6 K due to its gold coating. Most of the temperature gradient occurs along the thin rods. The total temperature rise is 36.4 K, as plotted in Figure 5c.

The noticeable resonance frequency shift with the temperature indicates that the torsional devices can be used as sensitive thermal detectors. We deposit a TiN film as an IR absorber by the magnetron sputtering method. Its IR reflection and transmission shows a strong function of the film thickness in the several-tens-of-nanometer range. The near-infrared absorption reaches a maximum 30% when the film thickness is about 15 nm.[13]

We use an all-optical system shown in Figure 1c to directly measure the NETD. To ensure that the heating arises predominantly from the infrared radiation, the intensity of the probing laser is kept at a minimal level as low as 33 nW. We characterized the IR response of a SiN torsional device covered by 20 nm sputtered TiN. The resonances in Figure 5d show a systematic redshift with the blackbody temperature. The fractional frequency shift is approximately 0.1% when the blackbody temperature rises from room temperature to 375 °C. The quality factor Q is about 913, remaining roughly constant over the temperature range. The resonant frequency reveals a quadratic relationship with the blackbody temperature as shown in Figure 5e. The nonlinear response of the device could be caused by the absorber which is wavelength selective for the incident infrared radiation. Using the Allan deviation $\sigma_A = 10^{-6}$ and the total frequency shift Δf = 750 Hz, a NETD = $(\Delta T_{bb} f_0 \sigma_A)/(\Delta f)$ = 390 mK is calculated, where ΔT_{bb} = 350 K is the total blackbody temperature variation. This temperature resolution is comparable with the reported NETD's of MEMS cantilever based IR detectors.[6,10,11]

There is still plenty of room to improve the NETD of these NEMS-based devices. The device thermal conductance can be lowered by 1 order of magnitude if α-Si is employed as the structural material. Another technical path is to improve the collection efficiency of the infrared optics by employing a low f-number IR lens. By adopting such technical innovations, we project that a NEMS-based frequency shift infrared bolometer should be able to reach a NETD < 10 mK.

In conclusion, we have demonstrated ultrahigh angular displacement, torque sensitivities, wide dynamic range (>100 dB), and superior frequency stability of nanoscale torsional resonators. We predict that the torsional resonator could be used as an ultrasensitive IR detector with achievable temperature resolution in the scene below 10 mK, and we have

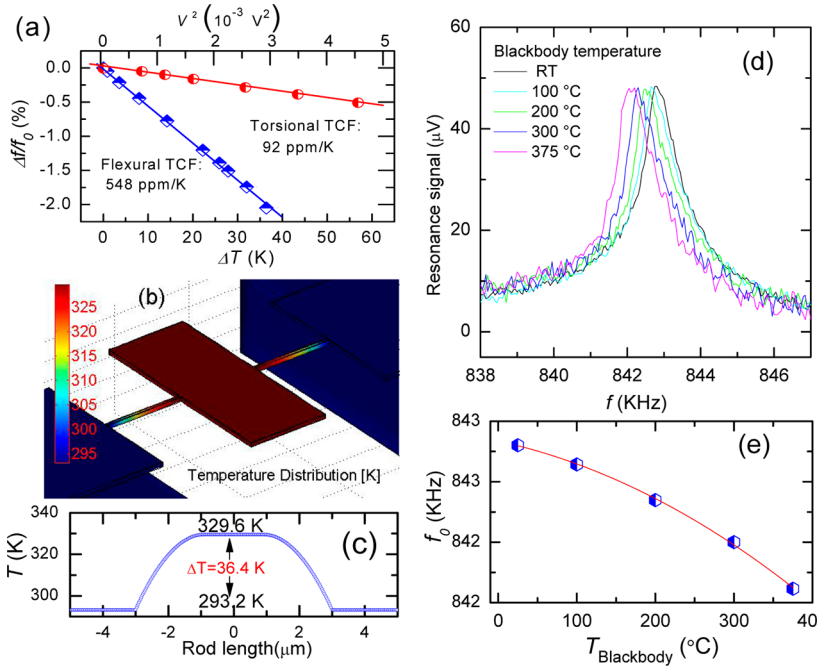

Figure 5. Thermal response study. (a) Relative frequency shift of the torsional (circles) and flexural (diamonds) mode versus the square of Joule heating voltage (top x-axis) and simulated temperature rise ΔT (bottom x-axis). (b) The simulated temperature distribution profile at a bias at 0.056 V. (c) Temperature profile along the center line of the device. (d) The IR response measurement shows the torsional resonances at various blackbody temperatures. (e) The resonant frequency as a function of blackbody temperature; the red curve is a parabolic fitting.

dx.doi.org/10.1021/nl304687p | Nano Lett. XXXX, XXX, XXX−XXX

demonstrated the first prototype devices based on very small paddle structures supported by thin nanorods, with significant promise for further scaling and optimization.

■ ASSOCIATED CONTENT

Supporting Information

Supporting theoretical modeling work on TCF, NETD, optical nonlinearity, and dynamic range of the torsional resonator and device fabrication techniques. This material is available free of charge via the Internet at http://pubs.acs.org.

■ AUTHOR INFORMATION

Corresponding Author

*E-mail: roukes@caltech.edu.

Notes

The authors declare no competing financial interest.

■ ACKNOWLEDGMENTS

We thank L.G. Villanueva for stimulating discussions, X. L. Feng for a critical reading of the manuscript, R. B. Karabalin for help in the optical measurement, D. Chi for assistance in electron beam lithography, and J. E. Sader acknowledges support from the Australian Research Council grants scheme. We are grateful for the support from DARPA/MTO under the Grant W31P4Q-10-1-0006.

■ REFERENCES

(1) Naik, A. K.; Hanay, M. S; Hiebert, W. K.; Feng, X. L.; Roukes, M. L. *Nat. Nanotechnol.* **2009**, *4*, 445−449.
(2) Rugar, D.; Budakian, R.; Mamin, H. J.; Chui, B. W. *Nature* **2004**, *430*, 329−332.
(3) O'Connell, A. D.; Hofheinz, M.; Ansmann, M.; Bialczak, R. C.; Lenander, M.; Lucero, E.; Neeley, M.; Sank, D.; Wang, H.; Weides, M.; Wenner, J.; Martinis, J. M.; Cleland, A. N. *Nature* **2010**, *464*, 697−703.
(4) Mertens, J.; Finot, E.; Thundat, T.; Fabre, A.; Nadal, M. H.; Eyraud, V.; Bourillot, E. *Ultramicroscopy* **2003**, *97*, 119−126.
(5) Larsen, T.; Schmid, S.; Grönberg, L.; Niskanen, A. O.; Hassel, J.; Dohn, S.; Boisen., A. *Appl. Phys. Lett.* **2011**, *98*, 121901.
(6) Zhao, Y.; Mao, M.; Horowitz, R.; Majumdar, A.; Varesi, J.; Norton, P.; Kitching, J. *J. Microelectromech. Syst.* **2002**, *11*, 136−146.
(7) Huang, S.; Tao, H.; Lin, I. K.; Zhang, X. *Sens. Actuators, A* **2008**, *145−146*, 231−240.
(8) Kao, P.; Tadigadapa, S. *Sens. Actuators, A* **2009**, *149*, 189−192.
(9) Jun, S. C.; Huang, X. M. H.; Manolidis, M.; Zorman, C. A.; Mehregany, M.; Hone, J. *Nanotechnology* **2006**, *17*, 1506−1511.
(10) Grbovic, D.; Lavrik, N. V.; Datskosa, P. G.; Forrai, D.; Nelson, E.; Devitt, J.; McIntyre, B. *Appl. Phys. Lett.* **2006**, *89*, 073118.
(11) Cheng, T.; Zhang, Q. C.; Wu, X. P.; Chen, D. P.; Jiao, B. B. *IEEE Electron Device Lett.* **2008**, *29*, 1218−1221.
(12) Attaf, N.; Aida, M. S.; Hadjeris, L. *Solid State Commun.* **2001**, *120*, 525−530.
(13) Valkonen, E.; Ribbing, C.-G.; Sundgren, J.-E. *Appl. Opt.* **1986**, *25*, 3624−3630.
(14) Uncooled Infrared Imaging Arrays and Systems. In *Semiconductors and Semimetals*; Krause, P. W., Skatrud, D. D., Eds.; Academic Press: San Diego, 1997; Vol. *47*.
(15) Cleland, A. N.; Roukes, M. L. *J. Appl. Phys.* **2002**, *92*, 2758−2769.
(16) Ekinci, K. L.; Yang, Y. T.; Roukes, M. L. *J. Appl. Phys.* **2004**, *95*, 2682−2689.
(17) Verbridge, S. S.; Parpia, J. M.; Reichenbach, R. B.; Bellan, L. M.; Craighead, H. G. *J. Appl. Phys.* **2006**, *99*, 124304.
(18) Irace, A.; Sarro, P. M. *Sens. Actuators* **1999**, *A21−A23*, 856−860.
(19) Pan, F.; Kubby, J. A.; Peeters, E.; Chen, J.; Vitomirov, O.; Taylor, D.; Mukherjee, S. *Proc. SPIE* **1997**, *3226*, 114−120.
(20) See Texas Instrument digital micromirror array DLP5500 datasheet, http://www.ti.com/lit/ds/symlink/dlp5500.pdf (accessed Oct 1, 2012).
(21) Evoy, S.; Carr, D. W.; Sekaric, L.; Olkhovets, A.; Parpia, J. M.; Craighead, H. G. *J. Appl. Phys.* **1999**, *86*, 6072−6077.
(22) Fennimore, A. M.; Yuzvinsky, T. D.; Han, W. Q.; Fuhrer, M. S.; Cumings, J.; Zettl, A. *Nature* **2003**, *424*, 408−410.
(23) Meyer, J. C.; Paillet, M.; Roth, S. *Science* **2005**, *309*, 1539−1541.
(24) Hall, A. R.; An, L.; Liu, J.; Vicci, L.; Falvo, M. R.; Superfine, R.; Washburn, S. *Phys. Rev. Lett.* **2006**, *96*, 256102.
(25) Cohen-Karrni, T.; Segev, L.; Srur-Lavi, O.; Cohen, S. R.; Joselevich, E. *Nat. Nanotechnol.* **2006**, *1*, 36−41.
(26) Hall, A. R.; Falvo, M. R.; Superfine, R.; Washburn, S. *Nat. Nanotechnol.* **2007**, *2*, 413−416.
(27) Papadakis, S. J.; Hall, A. R.; Williams, P. A.; Vicci, L.; Falvo, M. R.; Superfine, R.; Washburn, S. *Phys. Rev. Lett.* **2004**, *93*, 146101.
(28) Witkamp, B.; Poot, M.; Pathangi, H.; Hüttel, A. K.; Van der Zant, H. S. J. *Appl. Phys. Lett.* **2008**, *93*, 111909.
(29) Li, M.; Tang, H. X.; Roukes, M. L. *Nat. Nanotechnol.* **2007**, *2*, 114−120.
(30) Postma, H. W. Ch.; Kozinski, I.; Husain, A.; Roukes, M. L. *Appl. Phys. Lett.* **2005**, *86*, 223105.
(31) Hiebert, W. K.; Vick, D.; Sauer, V.; Freeman, M. R. *J. Micromech. Microeng.* **2010**, *20*, 115038.
(32) Antonio, D.; Pastoriza, H. *J. Microelectromech. Syst.* **2009**, *18*, 1396−1400.
(33) Allan, D. E. *Proc. IEEE* **1966**, *54*, 221−230.